

# Constructing Matching Cathode–Anode Interphases with Improved Chemo-mechanical Stability for High-Energy Batteries

Shiming Chen, Guorui Zheng,\* Xiangming Yao, Jinlin Xiao, Wenguang Zhao, Ke Li, Jianjun Fang, Zhuonan Jiang, Yuxiang Huang, Yuchen Ji, Kai Yang, Zu-Wei Yin, Meng Zhang, Feng Pan, and Luyi Yang\*



Cite This: *ACS Nano* 2024, 18, 6600–6611



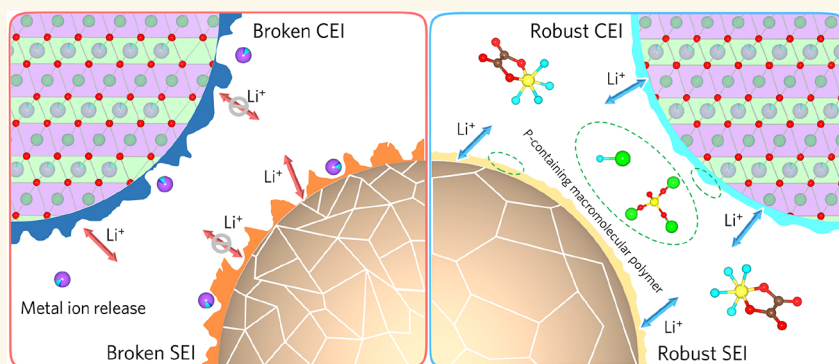
Read Online

ACCESS |

Metrics & More

Article Recommendations

Supporting Information



**ABSTRACT:** Coupling Ni-rich layered oxide cathodes with Si-based anodes is one of the most promising strategies to realize high-energy-density Li-ion batteries. However, unstable interfaces on both cathode and anode sides cause continuous parasitic reactions, resulting in structural degradation and capacity fading of full cells. Herein, lithium tetrafluoro(oxalato) phosphate is synthesized and applied as a multifunctional electrolyte additive to mitigate irreversible volume swing of the  $\text{SiO}_x$  anode and suppress undesirable interfacial evolution of the  $\text{LiNi}_{0.83}\text{Co}_{0.12}\text{Mn}_{0.05}\text{O}_2$  (NCM) cathode simultaneously, resulting in improved cycle life. Benefiting from its desirable redox thermodynamics and kinetics, the molecularly tailored additive facilitates matching interphases consisting of  $\text{LiF}$ ,  $\text{Li}_3\text{PO}_4$ , and P-containing macromolecular polymer on both the NCM cathode and  $\text{SiO}_x$  anode, respectively, modulating interfacial chemo-mechanical stability as well as charge transfer kinetics. More encouragingly, the proposed strategy enables 4.4 V 21700 cylindrical batteries (5 Ah) with excellent cycling stability (92.9% capacity retention after 300 cycles) under practical conditions. The key finding points out a fresh perspective on interfacial optimization for high-energy-density battery systems.

**KEYWORDS:** lithium-ion batteries, lithium tetrafluoro(oxalato) phosphate, electrolyte additive, solid-electrolyte interphase, cathode–electrolyte interphase

## INTRODUCTION

The continuous increasing demand of high-energy-density lithium-ion batteries (LIBs) has stimulated the development of high-capacity electrode materials.<sup>1–3</sup> In recent years, Ni-rich layered oxide  $\text{LiNi}_x\text{Co}_y\text{Mn}_{1-x-y}\text{O}_2$  (NCM,  $x > 0.5$ ) cathode and  $\text{SiO}_x$  ( $0 < x < 2$ ) anode materials have emerged as promising paired candidates owing to their high theoretical capacity and relatively low cost.<sup>4–7</sup> Nevertheless, both Ni-rich NCM and  $\text{SiO}_x$  electrodes suffer from severe capacity fading under high-voltage operations. For the NCM cathode, high-

voltage operation-derived high-capacity delivery could cause detrimental surface phase transformations into electrochemically inactive spinel and rock-salt structures. Additionally, the

**Received:** December 19, 2023

**Revised:** February 5, 2024

**Accepted:** February 8, 2024

**Published:** February 14, 2024



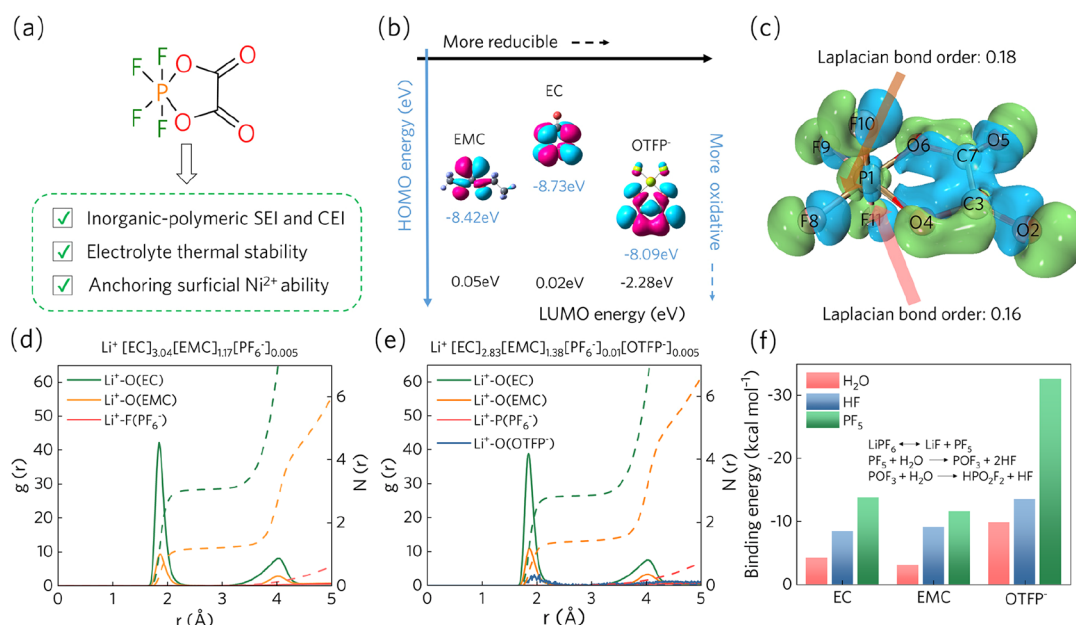


**Figure 1.** (a) Additive molecular advantages for high-energy-density batteries. (b) Diagram of calculated HOMO/LUMO energies (eV) of solvents and OTFP<sup>-</sup> anion. (c) Dual descriptor (DD) and Laplacian bond order (LBO) of OTFP<sup>-</sup> anion. Radial distribution functions (RDF) and corresponding coordination numbers ( $N(r)$ ) of BE electrolyte (d) and BE-LiOTFP electrolyte (e). (f) Binding energies of electrolyte molecules with H<sub>2</sub>O/HF/PF<sub>5</sub>, respectively.

accompanying active oxygen species release and low-valence transition metal (TM) ion dissolution could disrupt cathode–electrolyte interphase (CEI) layers as well as the interrelated solid–electrolyte interphase (SEI).<sup>8,9</sup> For the SiO<sub>x</sub> anode, its non-negligible volume swing (~118%) during the lithiation/delithiation process causes continuous consumption of electrolyte and results in SEI aging, which eventually impedes interfacial charge transfer.<sup>10,11</sup> Hence, for improvement from the outer surface to the inner bulk, constructing interface layers with desirable chemical and mechanical stability on both cathode and anode surfaces is vital to achieve high-energy-density batteries.<sup>12</sup>

Since typical commercial carbonate-based electrolytes are not suitable to form stable interface layers to simultaneously passivate the catalytic surface of Ni-rich cathodes and buffer the large volume change of Si-based anodes,<sup>13,14</sup> electrolyte modifications involving Li-salt, solvents, and/or additives have been extensively investigated as a cost-effective approach for battery performance optimization.<sup>15</sup> Especially, molecular-tailored sacrificial additives can be readily adopted to modify a currently existing electrolyte formula with better compatibility, showing excellent practicability.<sup>16</sup> For instance, positive electrode additives such as lithium difluorophosphate (LiDFP) could be oxidized on the NCM surface, participating in the formation of CEI being rich in lithium fluoride (LiF) and lithium phosphate (Li<sub>3</sub>PO<sub>4</sub>) compounds to suppress TM ion dissolution and cathode surface degradation,<sup>17</sup> whereas negative electrode additives such as fluoroethylene carbonate (FEC) was shown to help generate a lithium carbonate (Li<sub>2</sub>CO<sub>3</sub>) and LiF-abundant SEI on the surface of a Si-based anode at about 1.0 V (vs Li/Li<sup>+</sup>), which provides both improved mechanical stability and consequent interfacial Li<sup>+</sup> transfer.<sup>18,19</sup> As most reported additives focused on either cathode or anode side, their effectiveness in full cells needs further validation. Since there is a strong correlation on interface products between the cathode and paired anode, the

design of matching interfaces is critical for enabling full cells. Recently, bifunctional additives such as lithium difluorobis(oxalato)phosphate (LiDFBOP)<sup>20</sup> and tris(trimethylsilyl)phosphite (TMSP)<sup>21</sup> have been reported to ameliorate the interfacial issues of both cathodes and anodes. It is noteworthy that the film-forming ability of additives is mainly evaluated thermodynamically (i.e., redox potentials), but their reaction kinetics on each electrode is often neglected, which largely determine the formation of SEI/CEI layers and their chemomechanical properties for long-term cyclability. Therefore, designing an additive that constructs interphases with composition and morphology on both electrodes is highly desirable.

In this work, lithium tetrafluoro(oxalato)phosphate (LiOTFP) is introduced to the common baseline electrolyte (denoted as BE) consisting of 1 M LiPF<sub>6</sub> salt in the mixing solvents of ethylene carbonate (EC) and ethyl methyl carbonate (EMC) with a volume ratio of 3:7 for stabilizing both the NCM cathode and SiO<sub>x</sub> anode interfaces simultaneously (Figure 1a). With suitable redox thermodynamics and kinetics, LiOTFP facilitates robust CEI and SEI layers with similar chemical-morphological properties on NCM and SiO<sub>x</sub> electrodes, respectively. These chemically engineered SEI and CEI layers are found to not only stabilize the structures of active materials but also provide kinetically matched interphases for stable full-cell cycling. The fundamental principles of electrolyte engineering proposed in this work provide a way of thinking on developing high-energy-density batteries.

## RESULTS AND DISCUSSION

**LiOTFP Additive Influencing the Physicochemical Properties of Electrolyte.** Here, we synthesized a multifunction additive (LiOTFP) by heating of LiPF<sub>6</sub> reacted with lithium oxalate in dimethyl carbonate (more details in the Support information). The corresponding nuclear magnetic

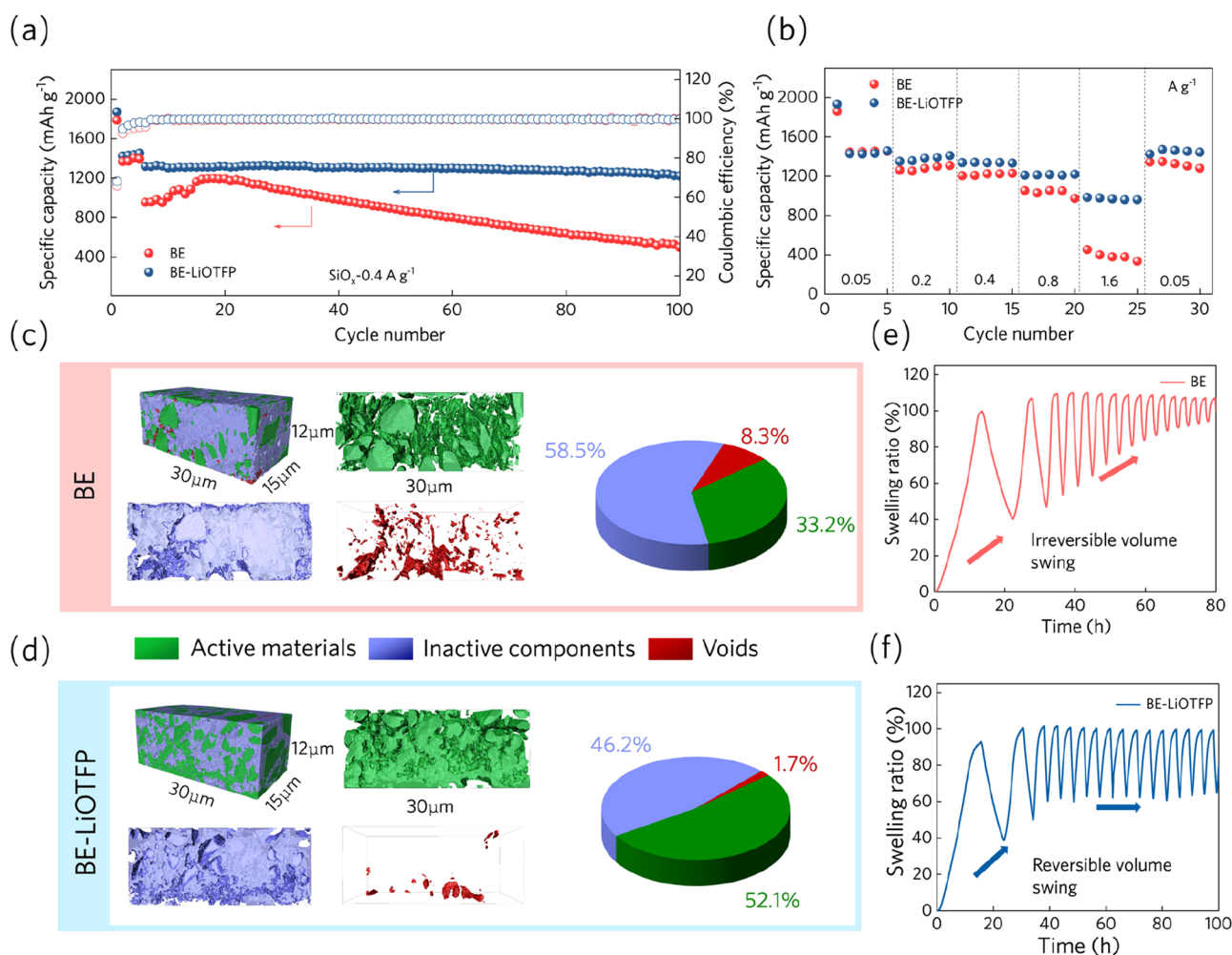


**Figure 2.** | (a) Galvanostatic cycling performance and Coulombic efficiency of  $\text{SiO}_x\|\text{Li}$  cells with BE and BE-LiOTFP electrolytes at a current density of  $0.05 \text{ A g}^{-1}$  for the first 5 cycles and  $0.4 \text{ A g}^{-1}$  for the subsequent cycles. (b) Rate performance of  $\text{SiO}_x\|\text{Li}$  cells with BE and BE-LiOTFP electrolytes. Three-dimensional image representation of  $\text{SiO}_x$  anodes in  $\text{SiO}_x\|\text{Li}$  cells with BE (c) and BE-LiOTFP (d) electrolytes after 100 cycles. The *in-situ* expansion ratio measurements of  $\text{SiO}_x$  anodes in  $\text{LiCoO}_2\|\text{SiO}_x$  cells with BE (e) and BE-LiOTFP (f) electrolytes for 16 cycles.

resonance (NMR) spectra (Figure S1) confirmed the formation of LiOTFP.<sup>22</sup> A computational approach was used to determine the highest occupied molecular orbital (HOMO) and lowest unoccupied molecular orbital (LUMO) energy levels of EC, EMC, and LiOTFP. As shown in Figure 1b, the LiOTFP additive exhibits higher HOMO energy and lower LUMO energy than solvents, suggesting its potential preferential redox reactions on both the cathode and anode sides. This could be further confirmed by comparing the linear sweep voltammetry curves (Figure S2), which show that the LiOTFP is oxidized on stainless steel at 4.0 V vs  $\text{Li}/\text{Li}^+$  to form a CEI and reduced on Cu at 2.0 V vs  $\text{Li}/\text{Li}^+$  to form an SEI, respectively. From the cyclic voltammogram (CV) curves of cells using BE or 0.5 wt % LiOTFP-containing electrolyte (denoted as BE-LiOTFP), the introduction of LiOTFP boosts the reaction kinetics of both NCM and  $\text{SiO}_x$  cells (Figure S3). In order to elucidate the electrochemical decomposition reaction kinetics of LiOTFP, the dual descriptor (DD) of the OTFP<sup>-</sup> anion is presented in Figure 1c, where the blue areas are prone to electrophilic attack and the green areas are prone to nucleophilic attack.<sup>23</sup> According to the Laplacian bond order (LBO) shown in Table S1, it is clear that the bond energies of four P–F bonds are relatively low and prone to be

attacked.<sup>24</sup> Interestingly, among these four P–F bonds, two of them (P1–F8 and P1–F9) tend to lose electrons, while the other two (P1–F10 and P1–F11) tend to gain electrons. Therefore, both oxidation and reduction reactions initiate from the breaking of P–F bonds, which potentially leads to similar decomposition products. More importantly, the similar bond energies of P–F bonds suggest well-matched decomposition kinetics of LiOTFP on the NCM cathode and  $\text{SiO}_x$  anode surface.

To investigate its influence on  $\text{Li}^+$  solvation structure, <sup>7</sup>Li NMR and Raman spectroscopy were carried out for the electrolytes with/without LiOTFP additive. NMR spectra of electrolytes (Figure S4) exhibit chemical shifts toward lower fields with the addition of LiOTFP, showing a weaker interaction of  $\text{Li}^+$  with solvents,<sup>25,26</sup> while the relative intensity of the solvated  $\text{PF}_6^-$  Raman peak increases (Figure S5), indicating more contact ion pairs (CIPs) are formed in the solvated structure of  $\text{Li}^+$  (i.e., more  $\text{PF}_6^-$  in the  $\text{Li}^+$  solvation sheath). In addition, the weakened  $\text{Li}^+$ –EC coordination is also evidenced by Fourier-transform infrared spectroscopy (FTIR) in BE-LiOTFP (Figure S6).<sup>27</sup> The atom-level solvation sheath of  $\text{Li}^+$  in both electrolytes was further investigated by molecular dynamics (MD) simulations (Figure

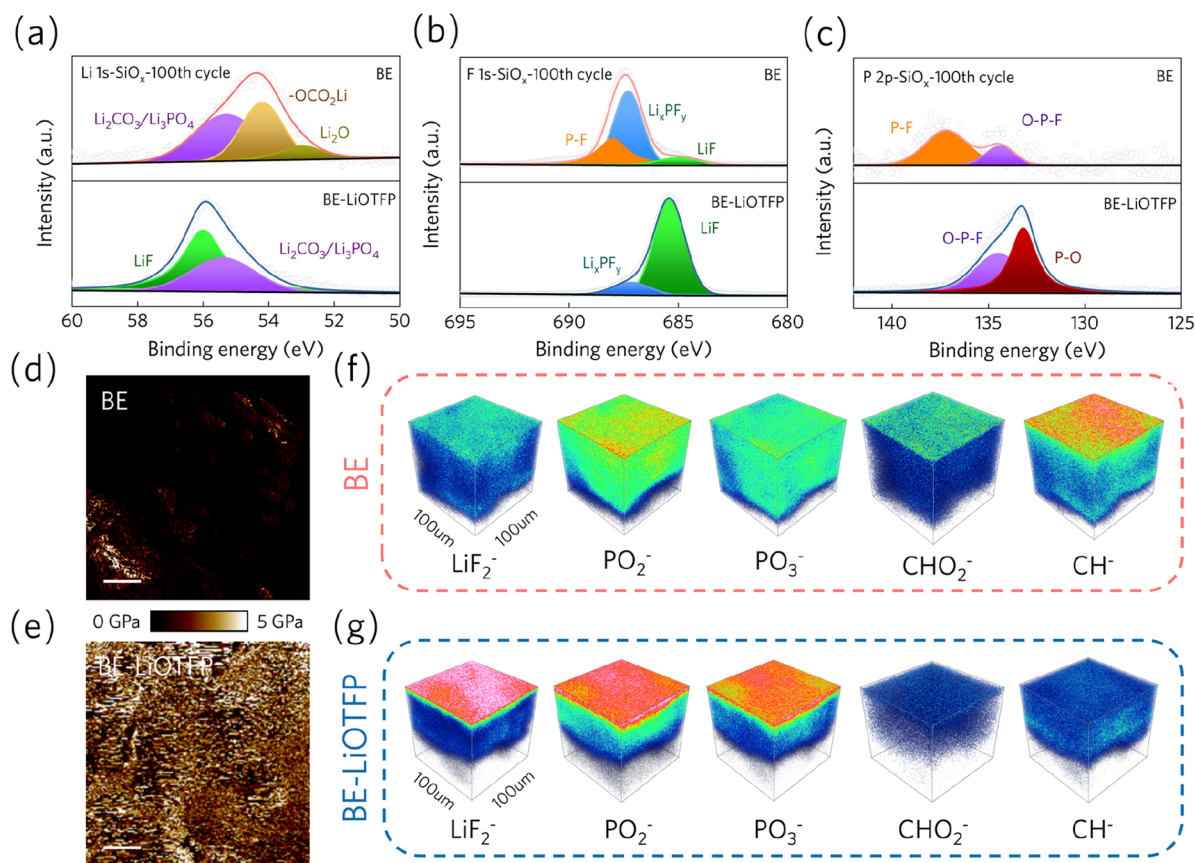


**Figure 3.** Li 1s (a), F 1s (b), and P 2p (c) X-ray photoelectron spectroscopy (XPS) spectra of  $\text{SiO}_x$  anodes in  $\text{SiO}_x\|\text{Li}$  cells with BE and BE-LiOTFP electrolytes after 100 cycles. Mechanical properties of the SEI on the surface of  $\text{SiO}_x$  anodes in  $\text{SiO}_x\|\text{Li}$  cells with BE (d) and BE-LiOTFP (e) measured via AFM (scale bar = 0.5  $\mu\text{m}$ ). The time-of-flight secondary ion mass spectrum (TOF-SIMS) three-dimensional distributions of  $\text{SiO}_x$  anodes in  $\text{NCM}\|\text{SiO}_x$  cells with BE (f) and BE-LiOTFP (g) electrolytes harvested after 100 cycles (the higher color saturation representing the higher content).

1d,e), which substantiates the above findings that  $\text{Li}^+$ –solvent interaction is notably weakened by LiOTFP additive: in BE, the coordination numbers of EC, EMC, and  $\text{PF}_6^-$  are 3.04, 1.17, and 0.005, respectively (Figure 1d), indicating that organic solvents dominate the solvation structure; with the addition of LiOTFP, the coordination number of EC reduces to 2.83, but the value of  $\text{PF}_6^-$  increases to 0.1, indicating enhanced  $\text{Li}^+$ – $\text{PF}_6^-$  interaction in the electrolyte. Moreover, the OTFP $^-$  anion is mainly located in the inner solvation sheath of  $\text{Li}^+$  with strong ion–ion interaction. Therefore, during initial cycles, OTFP $^-$  tends to participate in the very beginning formation reactions of the SEI/CEI. From the mean square displacement (MSD) of  $\text{Li}^+$  (Figure S7), it can also be concluded that  $\text{Li}^+$  diffuses faster in the BE-LiOTFP electrolyte.

Besides, the autocatalytic decomposition of  $\text{LiPF}_6$  leads to the formation of  $\text{LiF}$  and  $\text{PF}_5$ . And the trace amount of  $\text{H}_2\text{O}$  in the electrolyte will further react with  $\text{PF}_5/\text{LiPF}_6$  to produce acidic species such as HF, leading to severe damage of the SEI/CEI and battery degradation. As shown in Figure 1f, the binding energies between EC, EMC, and OTFP $^-$  with  $\text{H}_2\text{O}/\text{HF}/\text{PF}_5$  were calculated by density functional theory (DFT). The stronger binding interaction for OTFP $^-$  inhibits the hydrolysis reactions of  $\text{LiPF}_6$  and suppresses HF formation.<sup>28,29</sup> To verify this speculation, the high-temperature storage property of the electrolyte was tested. UV–vis spectra of both electrolytes before and after being stored at 45  $^\circ\text{C}$  for

one month are compared in Figure S8, where almost no change was detected in BE-LiOTFP throughout. In comparison, BE exhibits significant degradation, which could be attributed to HF formation according to the  $^{19}\text{F}$  NMR spectra (Figure S9). The above results confirm that LiOTFP could stabilize  $\text{PF}_5$  and mitigates the associated side-reactions.

**LiOTFP-Derived Robust Interphase Stabilizing  $\text{SiO}_x$  Anodes.** The galvanostatic cycling tests of  $\text{SiO}_x$  anodes (Figure 2a) show that BE-LiOTFP achieved a specific capacity of 1245  $\text{mA h g}^{-1}$  after 100 cycles, corresponding to a capacity retention of 94.5%, which outperforms BE (41.7% capacity retention). The corresponding  $dQ/dV$  curves after 100 cycles are extracted and compared (Figure S10). The peaks with lower intensity and larger voltage hysteresis in the BE system represent the sluggish (de)alloying reaction kinetics of  $\text{SiO}_x$  anodes.<sup>30</sup> The polarization of the  $\text{SiO}_x$  anode in BE electrolyte increased obviously due to the excessive pulverization. Under an elevated current density of 0.8  $\text{A g}^{-1}$  (Figure S11), high capacity retention could still be maintained in BE-LiOTFP (80.4% after 100 cycles). Moreover, the rate performance of  $\text{SiO}_x$  anodes is also enhanced in the presence of LiOTFP (Figure 2b and Figure S12). The improved electrochemical performance might be attributed to their well-preserved structural integrity.

Next, 3D structures of  $\text{SiO}_x$  anodes after 100 cycles were reconstructed by combining the focused ion beam and scanning electron microscope (FIB-SEM) techniques (Figure

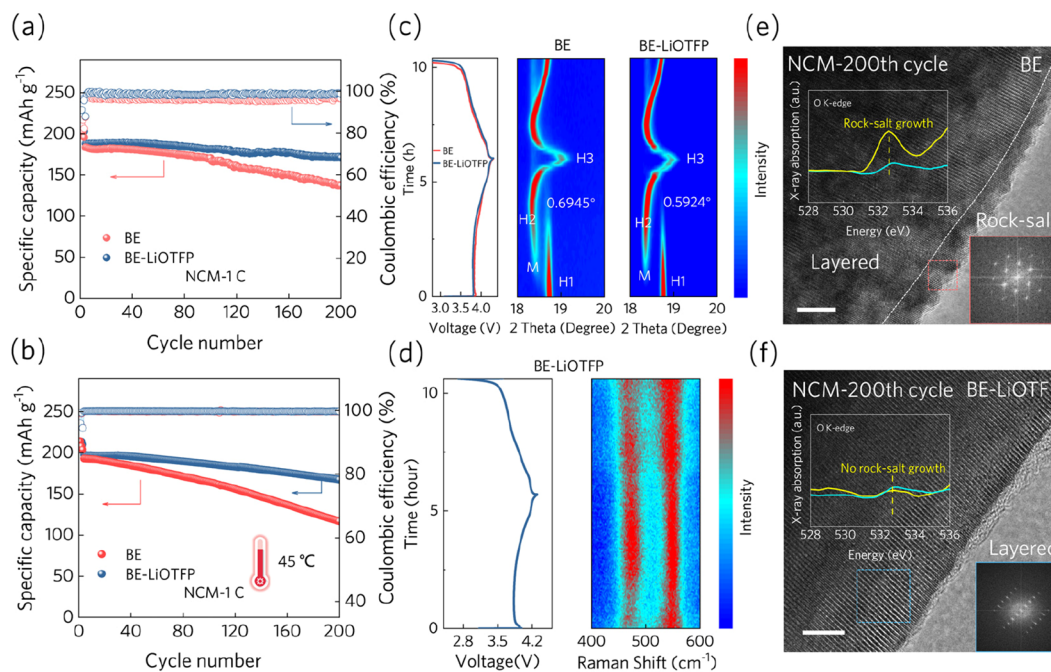


**Figure 4.** (a) Galvanostatic cycling performance and Coulombic efficiency of NCM//Li cells with BE and BE-LiOTFP electrolytes at a rate of 0.2 C for the first 3 cycles and 1 C for the subsequent cycles at 25 °C. (b) Galvanostatic cycling performance and Coulombic efficiency of NCM//Li cells with BE and BE-LiOTFP electrolytes at a rate of 0.2 C for the first 3 cycles and 1 C for the subsequent cycles at 45 °C. (c) *In-situ* XRD patterns of (003) peaks in the initial cycle for NCM//Li cells with BE and BE-LiOTFP electrolytes. (d) *In-situ* Raman spectra of NCM//Li cells with BE-LiOTFP electrolytes in the second cycle. FETEM images of NCM cathodes in NCM//Li cells with BE (e), BE-LiOTFP electrolytes (f) after 200 cycles (scale bar = 5 nm), and (insets) oxygen K-edge soft XAS results of NCM cathodes before cycling (cyan) and after 200 cycles (yellow) in TEY mode.

2c and d).<sup>31</sup> The selected region could be qualitatively and quantitatively divided into active materials (green), inactive components (blue), and voids (red).<sup>32</sup> The SiO<sub>x</sub> anode cycled with BE-LiOTFP contains 52.1 vol % active materials of the total components after cycling. In comparison, the anode cycled in BE exhibits only 33.2 vol % of particles. The increased inactive components and voids might be attributed to excess SEI accumulation and electrode disintegration. Further quantitative analysis demonstrates that the average volume of SiO<sub>x</sub> particles decreased drastically from 33.9 μm<sup>3</sup> to 6.07 μm<sup>3</sup> in BE, whereas the particles were much better preserved (15.1 μm<sup>3</sup>) in BE-LiOTFP (Table S2 and Table S3). In order to monitor the suppressing effect of LiOTFP on SiO<sub>x</sub> pulverization and expansion of the SiO<sub>x</sub> anodes in real time during cycling, *in-situ* expansion ratio measurements were conducted in electrochemical dilatometer cells (Figure S13). The swelling ratio curves of SiO<sub>x</sub> anodes (Figure 2e and f) clearly show that the volume swings in the cell using BE-LiOTFP tend to stabilize within 3 cycles, indicating good structural stability of the electrode inside. By contrast, the cell using BE exhibited continuously increasing irreversible volume changes, which might be attributed to the SiO<sub>x</sub> particles' fragmentation and uncontrolled SEI growth.<sup>33</sup> This result also agrees with the fluctuating Coulombic efficiency (CE) in the cell using BE during initial cycles (Figure 2a). Therefore, it can be speculated that LiOTFP additive helps to preserve the structural integrity of the SiO<sub>x</sub> anode by forming a mechanically stable SEI film that accommodates the volume changes during repeated cycling.

To explore the improving mechanisms of LiOTFP on interfaces, *in-situ* electrochemical impedance spectra (EIS) of SiO<sub>x</sub> anodes at the first cycle were recorded (Figure S14). A

large medium-frequency semicircle appears at 0.3 V in BE, suggesting an unstable interphase for Li<sup>+</sup> transfer owing to the volume swing. By contrast, the resistance of SEI and Li<sup>+</sup> charge transfer remained stable in BE-LiOTFP, indicating LiOTFP induced an SEI layer with lower interfacial resistance and superior cycling stability (Figure S15 and Table S4). The microstructure of the SEI formed in different electrolytes was further examined by cryo-transmission electron microscopy (cryo-TEM). After 100 cycles, a broken and uneven surface layer could be observed on the SiO<sub>x</sub> anode cycled in BE (Figure S16). By sharp contrast, the presence of LiOTFP additive results in a thin and uniform SEI layer, which could effectively passivate SiO<sub>x</sub> without compromising Li<sup>+</sup> transfer. The above morphological difference well agrees with the SEM images (Figure S17), where the electrode surface is smoother and denser for the SiO<sub>x</sub> anode cycled in BE-LiOTFP.

Additionally, Raman signals of amorphous Si can be measured on the SiO<sub>x</sub> anode cycled in BE (Figure S18), suggesting the presence of the poorly passivated SiO<sub>x</sub> surface. By sharp contrast, such a signal cannot be detected with the addition of LiOTFP, which corresponds to a fully passivated SiO<sub>x</sub> surface. X-ray photoelectron spectroscopy (XPS) was employed to analyze the chemical compositions of SEI layers. By combining Li 1s (Figure 3a), F 1s (Figure 3b), and P 2p (Figure 3c) spectra after 100 cycles, it could be concluded that much larger amounts of LiF and Li<sub>3</sub>PO<sub>4</sub> were formed in the SEI derived from BE-LiOTFP, which agrees with the diffraction spots observed in the cryo-TEM images (Figure S19).<sup>34</sup> C 1s spectra after 100 cycles (Figure S20) show that compared with a LiOTFP-containing electrolyte, the SiO<sub>x</sub> anode recovered from BE exhibits stronger -CO<sub>2</sub> signals, which derives from the continuous reduction decomposition of

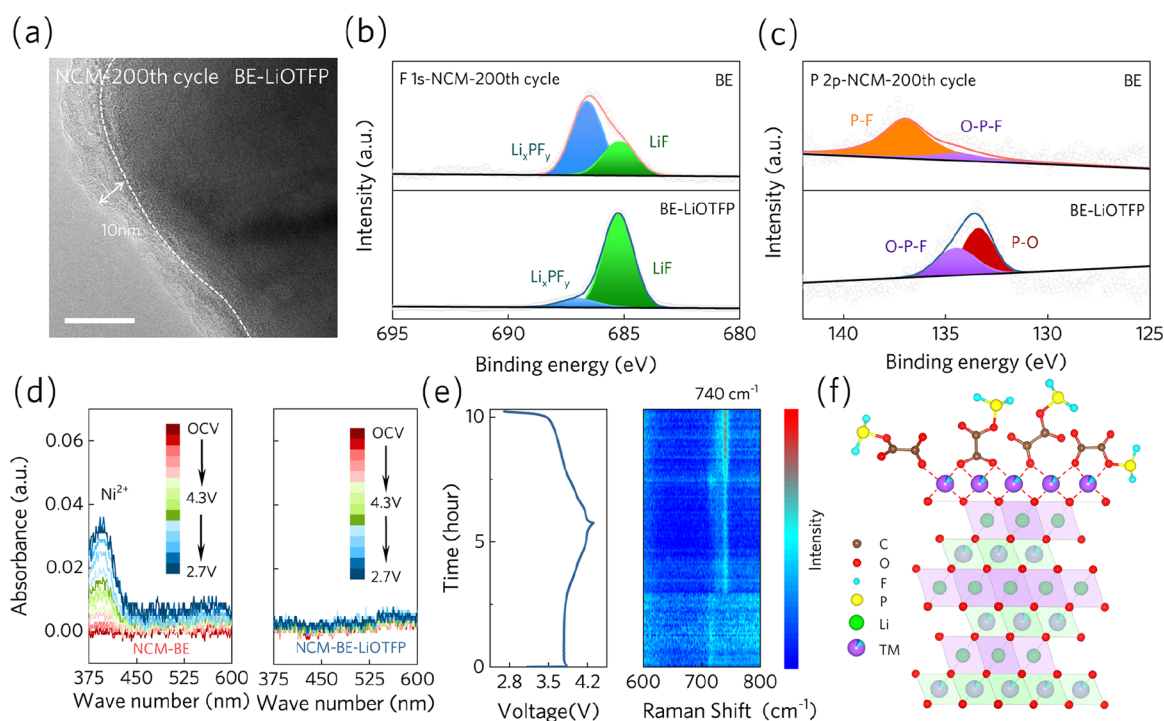


**Figure 5.** | (a) Cryo-TEM image and (insets) corresponding diffraction spots of NCM cathodes in NCM||Li cells with BE-LiOTFP electrolyte after 200 cycles (scale bar = 5 nm). F 1s (b) and P 2p (c) XPS spectra of NCM cathodes in NCM||Li cells with BE and BE-LiOTFP electrolytes after 200 cycles. (d) *In-situ* UV-vis spectra of NCM||Li cells with BE and BE-LiOTFP electrolytes during cycling. (e, f) Schematic diagram of suppressing Ni<sup>2+</sup> dissolution and corresponding *in-situ* Raman spectra.

carbonate solvents. The O K-edge soft X-ray absorption spectroscopy (XAS) in the TEY mode is surface sensitive ( $\sim 10$  nm), and it also confirms that there are more Li<sub>2</sub>CO<sub>3</sub> ( $\sim 534$  eV) and lithium carboxylate ( $\sim 544$  eV) species generated on the SiO<sub>x</sub> surface in the BE electrolyte (Figure S21).<sup>35</sup> As previously mentioned, LiOTFP could induce Li<sup>+</sup> to form CIP; therefore, an SEI dominated by anion-derived decomposition products is formed, which remained stable after long-term cycling when compared to the compositions formed after 5 cycles (Figure S22). This could be attributed to the fact that inorganic species (e.g., Li<sub>2</sub>CO<sub>3</sub>, LiF, and Li<sub>3</sub>PO<sub>4</sub>) have been reported to facilitate a mechanically robust SEI layer with high Li<sup>+</sup> conductivity.<sup>17,36</sup> Surface morphology and modulus were further measured by atomic force microscope (AFM) to evaluate the mechanical stability of different SEI layers. Compared with the surface morphology of a SiO<sub>x</sub> anode cycled in BE (Figure S23), a smoother surface can be obtained in BE-LiOTFP, inferring a homogeneous SEI layer. Moreover, the corresponding Derjaguin–Müller–Toporov (DMT) modulus of the SiO<sub>x</sub> anode cycled in BE-LiOTFP is significantly higher than that in BE, suggesting the improved mechanical strength of the SEI (Figure 3d and e). To further analyze the impact of LiOTFP on the compositional distribution of SEI layers, the time-of-flight secondary ion mass spectra (TOF-SIMS) of various fragment ions were acquired on cycled SiO<sub>x</sub> anodes (Figure 3f and g). In the presence of LiOTFP, intense signals of LiF<sub>2</sub><sup>-</sup>, PO<sub>3</sub><sup>-</sup>, and PO<sub>2</sub><sup>-</sup> were detected and focused within a thin layer in the 3D-rendering space, which suggests a thin and dense inorganic substance-dominant SEI covered in SiO<sub>x</sub> anodes with fast Li<sup>+</sup> conduction and excellent surface passivation. In contrast, BE results in a thick, loose, and inhomogeneous SEI that mainly consists of organic components (i.e., CHO<sub>2</sub><sup>-</sup>, CH<sup>-</sup>), indicating uncontrolled electrolyte

decomposition during cycling, then deteriorating reversibility of SiO<sub>x</sub> anodes. To conclude, we have found that LiOTFP additive helps to form a thin and mechanically robust SEI film abundant with Li-containing inorganic species (e.g., LiF and Li<sub>3</sub>PO<sub>4</sub>) on the SiO<sub>x</sub> anode interface, which can mechanically tolerate repeated volume swings and allows homogeneous and fast lithiation/delithiation on the SiO<sub>x</sub> surface, hence mitigating particle pulverization and repeated SEI growth, finally improving the cyclic stability and rate capability of the SiO<sub>x</sub> anode.

**LiOTFP-Dominant Interfacial Chemistry Modulation Stabilizing Ni-Rich Cathode.** Besides having an excellent effect on the SiO<sub>x</sub> anode, the impact of LiOTFP additive on the electrochemical performance of a Ni-rich NCM cathode was also investigated through galvanostatic cycling. As shown in Figure 4a, BE-LiOTFP enables a much higher specific capacity of 171 mA h g<sup>-1</sup> (corresponding to 91.4% capacity retention) than that cycled with baseline electrolyte (137 mA h g<sup>-1</sup>) after 200 cycles at 1 C. Compared to BE, an enhanced and stabilized CE was delivered with BE-LiOTFP. Since LiOTFP also promotes high temperature stability as mentioned above, the cycling performance of NCM cathodes was also evaluated at 45 °C (Figure 4b). The NCM cathode cycled with BE-LiOTFP achieves a specific capacity of 167 mAh g<sup>-1</sup> (corresponding to 84.7% capacity retention) after 200 cycles, while the capacity in BE fades rapidly as cycles go on. Similar to SiO<sub>x</sub> anodes, the NCM cathode cycled in BE-LiOTFP shows better rate performance at various C-rates (Figure S24 and Figure S25). By comparing the *in-situ* EIS of NCM cathodes at the first cycle, the resistance of CEI and Li<sup>+</sup> charge transfer remained stable under 4.3 V in the presence of LiOTFP, indicating a robust interphase formed on electrodes, while BE shows otherwise (Figure S26). Additionally, the

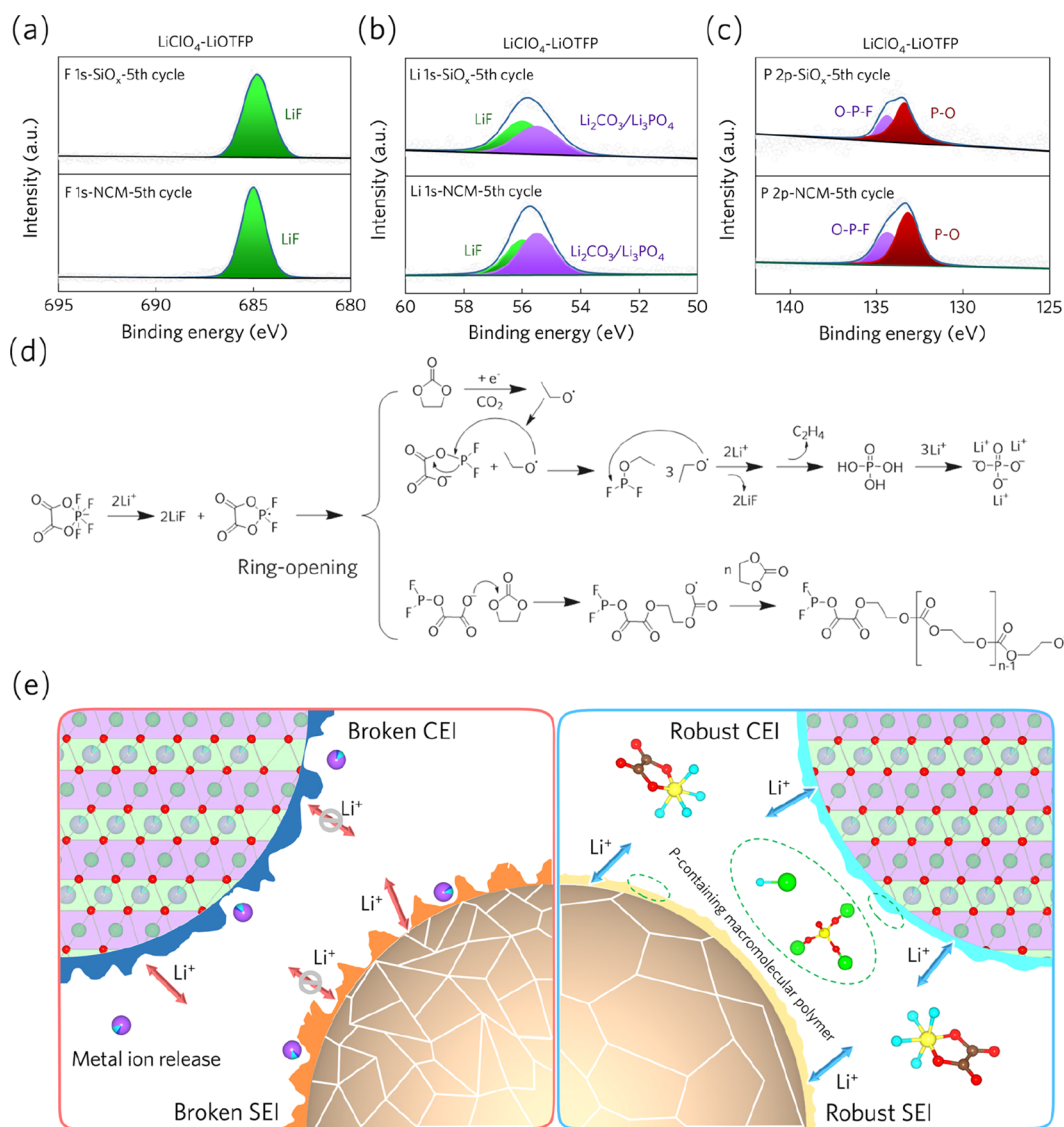


**Figure 6.** | F 1s (a), Li 1s (b), and P 2p (c) XPS spectra of SiO<sub>x</sub> anodes and NCM cathodes with LiClO<sub>4</sub> as Li-salt using LiOTFP after 5 cycles. (d) Proposed decomposition mechanism of LiOTFP at both cathode and anode sides. (e) Schematic illustration for the LiOTFP effect on the formation of the interphase layer on the anode and cathode surfaces.

addition of LiOTFP helps decrease the resistance of CEI and interfacial charge transfer after cycling (Figure S27 and Table S5), which also further explains the improved rate performance.

To understand the effects of LiOTFP on the structural stability of NCM cathodes, X-ray diffraction (XRD) patterns were acquired after 200 cycles (Figure S28). The lattice parameters *a* and *c* for the NCM cycled in BE-LiOTFP at the discharged state deviate less from the values of the pristine material than those for the NCM cycled in BE (Figure S29), indicating superior structural stability. The *in-situ* XRD analysis of NCM cathodes (Figure 4c) also confirms that the (003) peak shift of NCM cycled in BE-LiOTFP during the H<sub>2</sub>–H<sub>3</sub> transition (0.59°) is much lower than that cycled in BE (0.69°), suggesting a reduced shrinkage rate along the *c*-axis. According to the XRD and corresponding voltage profiles, we deduce that the smaller angle shift of the H<sub>2</sub>–H<sub>3</sub> phase transformation for the BE-LiOTFP electrolyte is caused by the formation of a stable interphase, hence the suppressed irreversible phase evolution.<sup>37,38</sup> To reveal the surface

structural evolution on the NCM cathode during cycling, *in-situ* Raman spectra (Figure 4d and Figure S30) of NCM cathodes were conducted. They exhibit two typical peaks centered at ~470 and 550 cm<sup>-1</sup>, which could be ascribed to the characteristic E<sub>g</sub> and A<sub>1g</sub> modes of the TM–O symmetrical stretching and the O–TM–O bending vibrations, respectively.<sup>39</sup> During cycling, both peaks remain almost unchanged in BE-LiOTFP, suggesting intact TM–O bonds, whereas BE results in fluctuating peak intensities at high voltages, indicating destabilization of TM–O bonds. High-resolution field-emission transmission electron microscopy (FETEM) images were also obtained for the cycled NCM particles (Figure 4e and f). In BE, a disordered rock-salt phase layer (~5 nm) was formed on the cathode surface. By contrast, the surficial layered structure is well-maintained in BE-LiOTFP, indicating that the surface degradation has been effectively suppressed. Besides, soft XAS was used to provide complementary structural information on NCM cathodes (insets in Figure 4e and f). A species at ~532.6 eV appeared after 200 cycles in BE, indicating the emergence of a rock-salt phase.<sup>17</sup>

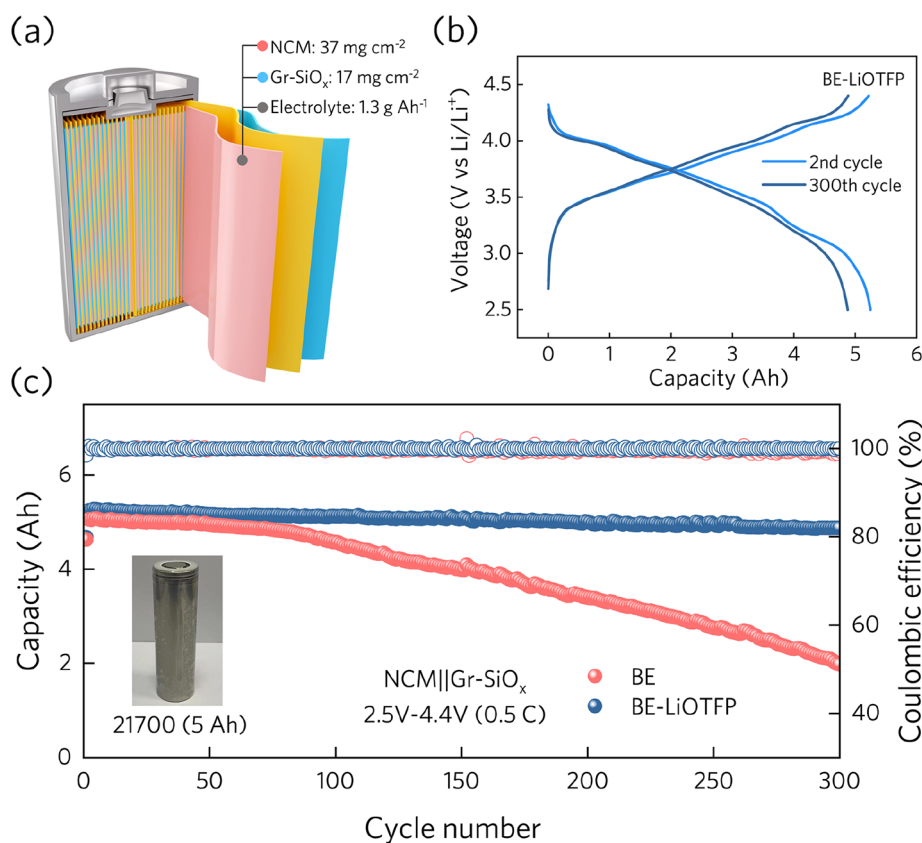


**Figure 7.** | (a) Schematic illustration of the LiOTFP effect on the formation of the interphase layer on the anodes and cathode surfaces. (b) Voltage profiles of 21700 cylindrical cells using BE-LiOTFP electrolyte. (c) Galvanostatic cycling performance and Coulombic efficiency of 21700 cylindrical cells at a rate of 0.5 C using BE and BE-LiOTFP electrolytes.

Additionally, cross-sectional SEM images (Figure S31) show that NCM secondary particles cycled in BE exhibit severe cracks, while only minor fissures can be found across the particles cycled in BE-LiOTFP. To sum up, it could be inferred that LiOTFP facilitates a robust CEI, which prevents the electrolyte from penetrating into the secondary particles and stabilizes surficial TM–O bonds, mitigating the degradation of cathode materials (Figure S32).

Then a series of characterizations were carried out aiming at dissecting the morphology and composition on the cathode surface. From cryo-TEM images (Figure 5a) of cycled NCM particles, it can be observed that a thin (~10 nm) and homogeneous CEI layer is found on the particle surface in BE-LiOTFP, leading to its superior structural stability for mitigating the surface degradation of the cathode material. After 200 cycles in BE, the NCM particle was coated with fragmented and uneven deposits, failing to completely passivate the NCM surface (Figure S33).<sup>40,41</sup> These results are supported by the top-view SEM images of cycled cathodes (Figure S34), where LiOTFP leads to a smooth surface, while a porous surface structure is formed in BE. XPS analysis was further conducted to investigate the component information on the CEI. The intensified signal of the LiF indicates that LiOTFP decomposes to help form a robust CEI on the NCM side (Figure 5b). In comparison, the CEI on the surface of NCM cycled in BE electrolyte contains a large amount of alkyl lithium that originates from the excessive decomposition of the electrolyte solvent and LiPF<sub>6</sub> (Figure S35). The peak at 133.2 eV in the P 2p spectra (Figure 5c) also confirms the presence of –PO<sub>2</sub> and –PO<sub>3</sub> in the CEI derived from LiOTFP

decomposition. Similar to the SiO<sub>x</sub> anode, a robust CEI dominated by OTFP<sup>–</sup> anion-derived decomposition products was formed on the Ni-rich NCM cathode, which remained stable and contributed to inhibit TM dissolution after long-term cycling when compared to what was detected after only 3 cycles (Figure S36).

TM dissolution from the cathode and the subsequent migration to the anode surface have been reported to severely degrade overall electrochemical performance. Therefore, *in-situ* ultraviolet–visible (UV–vis) spectroscopy testing was performed in a designed cell (see configuration in Figure S37) to observe TM dissolution. For BE, a peak associated with dissolved Ni<sup>2+</sup> (375–400 nm) emerged at a very early stage and quickly intensified during cycling. In contrast, BE-LiOTFP shows no apparent absorption peak (Figure 5d). Both XPS spectra of Ni 2p (Figure S38) and the depth profile of the Ni<sup>–</sup> fragment (Figure S39) obtained from postcycling anodes also confirmed that Ni dissolution in LiOTFP-containing electrolyte is greatly constrained. To probe the relevant mechanism of stabilizing transition metal ions in NCM, *in-situ* Raman spectroscopy was performed to monitor the surface evolution. It is clearly shown that a peak at ~740 cm<sup>–1</sup> emerged around 3.9 V during charging (Figure 5e), which could be assigned to the Ni–O ionic bond formed through coordination between Ni<sup>2+</sup> and the ring-opened product of the OTFP<sup>–</sup> anion based on DFT calculation (Figure S40). According to the above results, it can be inferred that upon oxidation, OTFP<sup>–</sup> forms coordinating species that anchor surficial Ni through Ni–O complexing (Figure 5f), which not only inhibits Ni dissolution into the electrolyte but also passivates the NCM surface at the

molecular level, hence resulting in the well-preserved electrode structure.

**The Improved Mechanism of LiOTFP Additive in Full Cells.** As LiOTFP also enables more  $\text{PF}_6^-$  in the  $\text{Li}^+$  solvation sheath, the interference of  $\text{LiPF}_6$  should be excluded in order to investigate the decomposition mechanisms of LiOTFP as an additive. In this case, lithium perchlorate ( $\text{LiClO}_4$ ) was employed to replace  $\text{LiPF}_6$  as the electrolytic salt. Both the  $\text{SiO}_x$  anode and NCM cathode cycled with this electrolyte were examined through XPS. In the F 1s spectra (Figure 6a), the LiF peak can be clearly observed on both the cathode and anode sides, which directly demonstrates the participation of LiOTFP in the formation of SEI/CEI layers. Both the Li 1s (Figure 6b) and P 2p (Figure 6c) spectra demonstrate a substantial amount of  $\text{Li}_3\text{PO}_4$  generated on the surfaces of both electrodes. Based on the above experimental results and theoretical calculations, detailed decomposition mechanisms of LiOTFP are proposed in Figure 6d. In detail, the OTFP anion consists of an oxalic ring and four P–F bonds, which generate LiF-rich species through the prior defluorination. Among these four P–F bonds, two of them tend to lose electrons and the other two tend to gain electrons. Then the  $\text{C}_2\text{O}_4\text{PF}_2$  radical is ring-opened and the P–O bond is broken, forming an interface layer with  $\text{Li}_3\text{PO}_4$  and P-containing polymeric species. In addition, the cell using 0.5 wt % LiOTFP showed better electrochemical performance compared to 1 wt % LiOTFP (Figure S41). It is speculated that the excess LiOTFP could lead to the formation of HF.<sup>17</sup>

Combining all the above results, the role of LiOTFP in mitigating interfacial issues for NCM and  $\text{SiO}_x$  can be schematically illustrated (Figure 6e): during the decomposition process, matching interface layers with high chemical and mechanical stability are generated on both electrodes. For  $\text{SiO}_x$  anodes, the LiF-rich interface layer helps to accommodate drastic deformation of anodes due to the high Young's modulus and low adhesion to the alloy surface.<sup>42,43</sup> Additionally, the simultaneously formed P-containing polymeric species serve as a binder that integrates inorganic components into a homogeneous layer with desirable mechanical durability, suppressing  $\text{SiO}_x$  anode expansion and disintegration. For NCM cathodes, the stable passivating interphase prevents the surface and bulk structural degradation (e.g., side reactions and TM dissolution) by anchoring surficial  $\text{Ni}^{2+}$  through Ni–O complexation at the molecular level. Besides, the generation of  $\text{Li}_3\text{PO}_4$  leads to a fast ionic transport and low interphase impedance due to its high ionic conductivity.

As previously reported,<sup>44</sup> similar compositions and morphology of CEI and SEI could improve the cycling stability of full cells synergistically due to the strong interaction effects between them. The kinetics of the SEI and the CEI were also tested by the electrochemical method. As shown in Figure S42 and Figure S43, the activation energies of the SEI (43.2 kJ mol<sup>-1</sup>) and CEI (37.4 kJ mol<sup>-1</sup>) in BE-LiOTFP are lower than those in BE, indicating excellent kinetics of the SEI formed in LiOTFP-containing electrolyte. Therefore, the robust SEI and CEI with similar compositions formed in BE-LiOTFP not only stabilize the structural stability but also provide well-matched interfacial charge transfer kinetics of the  $\text{SiO}_x$  anode and NCM cathode in full cells.<sup>45,46</sup> To further demonstrate the advantage of the symmetric SEI–CEI coupling under practical testing conditions, proof-of-concept NCM||Gr- $\text{SiO}_x$  cylindrical cells (~5 Ah) were assembled and tested between 2.5 and 4.4 V (Figure 7a). The cylindrical cells were tested with lean

electrolytes (1.3 g Ah<sup>-1</sup>) and an N/P ratio (the capacity ratio of the negative electrode to the positive electrode) of 1.08. The LiOTFP-derived interface layer protects the full cell from voltage fading after 300 cycles: the decay of discharge middle voltage in BE ( $\Delta V_{\text{BE}} = -0.13$  V) is also faster than that in BE-LiOTFP ( $\Delta V_{\text{BE-LiOTFP}} = -0.02$  V) due to the irreversible phase transition and the increased interfacial resistance (Figure 7b and Figure S44). Moreover, BE-LiOTFP delivered a high capacity retention of 92.9% and average CE of 99.95% after long-term cycling (Figure 7c). In comparison, the cylindrical cell with BE showed serious deterioration during the long-term cycling, leading to a capacity retention of merely 39%. The cycling performance comparison with the previously reported electrolyte additives (Table S6) demonstrates the excellent potential of LiOTFP to construct the chemo-mechanically stable interphases for high-energy batteries.

## CONCLUSION

In this work, through introducing the designed ionic additive LiOTFP into the electrolyte, an efficient approach to improve both the  $\text{SiO}_x$  anode and NCM cathode is reported. Exhibiting suitable redox potentials and kinetics, LiOTFP facilitates thin yet robust interfacial layers consisting of LiF,  $\text{Li}_3\text{PO}_4$ , and P-containing polymeric species symmetrically on both electrodes. The electrochemically tailored interphases not only provide favorable mechanical properties to avoid irreversible volume changes of the  $\text{SiO}_x$  anode but also chemically anchor surficial TM to inhibit its dissolution from the NCM cathode. Consequently, improved long-term cycling performance can be obtained for both electrodes. Moreover, the well-matched SEI–CEI pair enables coordinated interfacial charge transfer kinetics and chemo-mechanical stability, resulting in an impressive capacity retention of 92.9% based on a 21700 cylindrical cell. The key findings in this study provide the guidance for electrolyte additive design of high-energy-density batteries.

## EXPERIMENTAL SECTION

**Materials.** Polyacrylic acid, N-methylpyrrolidone, and polyvinylidene fluoride were purchased from Aladdin. Lithium tetrafluoro(oxalato)phosphate, dimethyl carbonate, and dichloromethane were purchased from Innochem. Microsized  $\text{SiO}_x$  was kindly provided by Shenzhen BTR New Material Group Co., Ltd., and  $\text{Li-Ni}_{0.83}\text{Co}_{0.12}\text{Mn}_{0.05}\text{O}_2$  powder was purchased from Zhejiang Hitrans Lithium Technology Co., Ltd. The baseline electrolyte was obtained from DoDoChem (Suzhou, China). Freshly deionized water was used in experiments.

**Synthesis of Lithium Tetrafluoro(oxalato)phosphate.** LiOTFP was synthesized by heating  $\text{LiPF}_6$  at 200 °C to generate  $\text{PF}_5$  gas and transferred into a suspension of lithium oxalate in dimethyl carbonate at 25 °C. The mixture was stirred vigorously at 25 °C for 4 h, and the lithium salt was purified by repeated recrystallization from 1:1 (v/v) dimethyl carbonate/dichloromethane.

**Preparation of Electrodes.** The  $\text{SiO}_x$  anodes were made by a typical slurry casting method with active materials ( $\text{SiO}_x$ ), conductive carbon (acetylene black), and binder (poly(acrylic acid)) at a mass ratio of 8:1:1. The slurry was casted onto a Cu foil current collector and dried in a vacuum at 100 °C overnight. Then electrodes were cut into disks with a diameter of 10 mm. The typical mass loading of active materials on the anode was  $1.5 \pm 0.2$  mg cm<sup>-2</sup>. The  $\text{LiNi}_{0.83}\text{Co}_{0.12}\text{Mn}_{0.05}\text{O}_2$  and  $\text{LiCoO}_2$  cathodes consist of the mixture of active materials, acetylene black, and polyvinylidene fluoride in a weight ratio of 8:1:1 coated onto an Al current collector. The typical mass loading of active materials on the cathode was  $2 \pm 0.2$  mg cm<sup>-2</sup>. The baseline electrolyte is composed of 1.0 M  $\text{LiPF}_6$  in 3:7 (v/v) EC/

EMC. LiOTFP was chosen as the electrolyte additive (0.5 wt %) for the experimental group. The separator was porous PP films (Celgard 2500). Full cells were assembled using the same electrolyte and separator as those used in the half-cells. The 21700 cylindrical cells consist of  $\text{LiNi}_{0.83}\text{Co}_{0.12}\text{Mn}_{0.05}\text{O}_2$  cathodes and graphite anodes (containing 5%  $\text{SiO}_x$ ).

**Electrochemical Measurements.** The cycling tests were carried out using a Neware battery test system within the voltage range of 0.01–1 V (vs  $\text{Li}/\text{Li}^+$ ) for the  $\text{SiO}_x$  anodes and 2.7–4.3 V (vs  $\text{Li}/\text{Li}^+$ ) for the  $\text{LiNi}_{0.83}\text{Co}_{0.12}\text{Mn}_{0.05}\text{O}_2$  cathodes. The 21700 cylindrical cells were cycled within the voltage range of 2.5–4.2 V for the first cycle and 2.5–4.4 V for the subsequent long cycle. The linear sweep voltammetry (LSV) measurement scanning rate was  $0.1 \text{ mV s}^{-1}$ . CVs of experiments were conducted at a scan rate of  $0.1 \text{ mV s}^{-1}$  for various electrodes in the respective test voltage range. The EIS experiments were performed on an electrochemical workstation (CHI 660E) in the frequency range of 0.01 Hz to 1 MHz. *In-situ* EIS measurements were done under the current density of 0.2 C.

**Material Characterizations.** XRD patterns of the prepared samples were collected by using a Bruker D8 Advance diffractometer with a  $\text{Cu K}\alpha$  radiation source ( $\lambda = 0.154 \text{ nm}$ ). The soft X-ray absorption spectroscopy (sXAS) experiments at the O K-edge were measured at beamline 02B02 at Shanghai Synchrotron Radiation Facility (SSRF). The cycled samples were sealed in argon-filled sample holders to avoid air and moisture contamination. The size of  $\text{SiO}_x$  particles was measured by a Mastersizer 3000. A Bruker Multimode 8 AFM was applied to test the surface morphology and modulus of the solid–electrolyte interphase. FESEM (ZEISS SUPRA55, Carl Zeiss) was used to observe the top-view morphology of electrodes. The cross-section images of the electrodes were obtained using focused ion beam (FEI Scios-ZEISS SUPRA 55) equipment. High-resolution FETEM (JEOL-3200FS) was used to study the structure of materials. The observation of an interphase layer for samples was done in a  $-172 \text{ }^\circ\text{C}$  environment by a cryo transfer tomography holder (model 2550, Fischione).  $^7\text{Li}$  NMR and  $^{19}\text{F}$  NMR were recorded on a Quantum-I Plus 400 MHz NMR spectrometer at 298 K. FTIR spectra were collected on a Nicolet Avatar 360 spectrophotometer (ATR). The change in chemical state of electrodes with different electrochemical status was analyzed by XPS (ESCALAB 250Xi). All the samples were transferred in a vacuum, and the base pressure of the sample chamber was kept below  $3.0 \times 10^{-10}$  mbar during XPS measurements. A TOF-SIMS was measured on an ION-TOF GmbH TOF-SIMS 5-100 spectrometer. The analysis chamber was maintained in ultrahigh vacuum at a pressure below  $2 \times 10^{-9}$  mbar, and a 500 eV  $\text{Cs}^+$  ion beam was applied for sputtering the cycled  $\text{SiO}_x$  electrodes in the full cells for depth profiling. The typical sputtering area was  $100 \times 100 \text{ }\mu\text{m}$ . *In-situ* Raman measurements were taken by a Renishaw InVia Raman microscope with a 633 nm laser, which irradiates the surface of the cathode through Li metal foil and a glass fiber separator with a 2 mm radius hole. Galvanostatic measurements were performed at 0.2 C within the voltage range of 2.7–4.3 V for Li ||  $\text{LiNi}_{0.83}\text{Co}_{0.12}\text{Mn}_{0.05}\text{O}_2$  cells while the Raman signals were recorded simultaneously. *In-situ* UV–vis data were collected on a UV–vis spectrophotometer (Shimadzu UV-2450). The cuvette was adopted as an electrochemical cell. The reference cuvette was only filled with electrolyte. The entire assembly process was in an Ar-filled glovebox, and the cuvettes were sealed up with Teflon tape. The 3D SEM-FIB image reconstruction data of  $\text{SiO}_x$  anodes were collected by Auto Slice and View software (FEI, Scios). After collecting cross-sectional images of each sample, alignment, segmentation, cropping, and labeling of 3D reconstructions were performed by Avizo software, which was also used to quantify various microstructural features of the 3D reconstruction of the sample. The T1 mode was used for acquisition of electron beam images at the early stage of this three-dimensional reconstruction, and the different components could be identified and segmented according to image contrast. The *in-situ* swelling ratio (%) tests during cycling of the electrode were performed at Shenzhen BTR New Material Group Co., Ltd. The experimental device is composed of a measuring table, electrolytic cell, and displacement sensor. The

$\text{SiO}_x$  anodes expanded and pushed the electrode stopper upward. The displacement sensor outside of the electrolytic cell could detect real-time displacement change.

**Theoretical Calculation.** All calculations were based on the Gaussian 09 package with the DFT method. The B3PW91/6-311++G\*\* theory level was used to optimize the molecular structure and perform frequency analysis. The polarized continuum model (PCM) was used to describe the implicit solvent effect on the reduction and oxidation processes of the additives. Eps constant of EC (89.6) and epsinf constant of EC (1.9) were used for all PCM calculations. We used the PBE1PBE/6-311++G\*\* theory level for the C, O, P, and F atoms in the calculation of the theoretical Raman spectra. The split-valence-shell Gaussian basis set SDD was used for transition metal atoms. The frequency scale factor was set at 0.95 for the electronic model chemistries. The Laplacian bond order of the OTFP<sup>−</sup> anion was calculated based on the Multiwfn program developed by Lu et al.<sup>47</sup> The binding energy with the corrections of basis set superposition error considered was calculated by the following equation:

$$E_{\text{binding}} = E_{\text{totally}} - E_x - E_y + E_{\text{BSSE}}$$

All MD simulations were conducted by the Large Scale Atomic/Molecular Massively Parallel Simulator (LAMMPS). The simulation boxes were filled with 50  $\text{LiPF}_6$  + 225 EC + 338 EMC (baseline electrolyte) and 50  $\text{LiPF}_6$  + 225 EC + 338 EMC + 2 LiOTFP (LiOTFP-containing electrolyte). The systems were equilibrated at 300 K in the isothermal–isobaric (NPT) ensemble for 5 ns using the Parrinello–Rahman barostat to maintain a pressure of 1 bar and a temperature of 300 K with a time constant of 1 ps. Finally, another 10 ns simulation in an NVT ensemble under Nose-Hoover thermostats at 300 K was performed.

## ASSOCIATED CONTENT

### Supporting Information

The Supporting Information is available free of charge at <https://pubs.acs.org/doi/10.1021/acsnano.3c12823>.

Characterizations of different electrolytes such as LSV curves,  $^7\text{Li}$  NMR spectra,  $^{19}\text{F}$  NMR spectra, Raman spectra, FTIR spectra, and UV–vis spectra; MD simulation results; characterizations of  $\text{SiO}_x$  anodes and NCM cathodes such as CV curves, galvanostatic charge–discharge curves, *in-situ* EIS, variable-temperature impedance, cryo-TEM images, SEM images, XPS spectra, and Raman spectra; AFM results of  $\text{SiO}_x$  anodes; XRD patterns of NCM cathodes (PDF)

## AUTHOR INFORMATION

### Corresponding Authors

Guorui Zheng – Institute of Materials Research (IMR), Tsinghua Shenzhen International Graduate School, Tsinghua University, Shenzhen 518055, People's Republic of China; Email: [zhengguorui1991@163.com](mailto:zhengguorui1991@163.com)

Luyi Yang – School of Advanced Materials, Peking University Shenzhen Graduate School, Shenzhen 518055, People's Republic of China; [orcid.org/0000-0002-5516-9829](https://orcid.org/0000-0002-5516-9829); Email: [yangly@pkusz.edu.cn](mailto:yangly@pkusz.edu.cn)

### Authors

Shiming Chen – School of Advanced Materials, Peking University Shenzhen Graduate School, Shenzhen 518055, People's Republic of China

Xiangming Yao – School of Advanced Materials, Peking University Shenzhen Graduate School, Shenzhen 518055, People's Republic of China

Jinlin Xiao – BTR New Material Group Co., Ltd., Shenzhen 518107, People's Republic of China

Wenguang Zhao – School of Advanced Materials, Peking University Shenzhen Graduate School, Shenzhen 518055, People's Republic of China

Ke Li – School of Advanced Materials, Peking University Shenzhen Graduate School, Shenzhen 518055, People's Republic of China

Jianjun Fang – School of Advanced Materials, Peking University Shenzhen Graduate School, Shenzhen 518055, People's Republic of China

Zhuonan Jiang – School of Advanced Materials, Peking University Shenzhen Graduate School, Shenzhen 518055, People's Republic of China

Yuxiang Huang – School of Advanced Materials, Peking University Shenzhen Graduate School, Shenzhen 518055, People's Republic of China

Yuchen Ji – School of Advanced Materials, Peking University Shenzhen Graduate School, Shenzhen 518055, People's Republic of China

Kai Yang – Advanced Technology Institute, University of Surrey, Guildford, Surrey GU2 7XH, U.K.; [orcid.org/0000-0001-7391-1495](https://orcid.org/0000-0001-7391-1495)

Zu-Wei Yin – College of Energy, Xiamen University, Xiamen 361005, People's Republic of China; [orcid.org/0000-0002-0728-1154](https://orcid.org/0000-0002-0728-1154)

Meng Zhang – BTR New Material Group Co., Ltd., Shenzhen 518107, People's Republic of China; [orcid.org/0000-0003-4713-4375](https://orcid.org/0000-0003-4713-4375)

Feng Pan – School of Advanced Materials, Peking University Shenzhen Graduate School, Shenzhen 518055, People's Republic of China; [orcid.org/0000-0002-8216-1339](https://orcid.org/0000-0002-8216-1339)

Complete contact information is available at:  
<https://pubs.acs.org/10.1021/acsnano.3c12823>

## Author Contributions

S.C. and G.Z. contributed equally to this work.

## Notes

The authors declare no competing financial interest.

## ACKNOWLEDGMENTS

This work was financially supported by Shenzhen Science and Technology Research Grant (No. ZDSYS201707281026184). The authors thank Shanghai Synchrotron Radiation Facility (SSRF) (beamline 02B02) for the allocation of synchrotron beam time.

## REFERENCES

- (1) Choi, J. W.; Aurbach, D. Promise and Reality of Post-Lithium-Ion Batteries with High Energy Densities. *Nat. Rev. Mater.* **2016**, *1*, 1–16.
- (2) Zheng, J.; Ye, Y.; Pan, F. Structure Units” as Material Genes in Cathode Materials for Lithium-Ion Batteries. *Natl. Sci. Rev.* **2020**, *7* (2), 243.
- (3) Zhang, X.; Wang, A.; Liu, X.; Luo, J. Dendrites in Lithium Metal Anodes: Suppression, Regulation, and Elimination. *Acc. Chem. Res.* **2019**, *52* (11), 3223–3232.
- (4) Liu, Z.; Yu, Q.; Zhao, Y.; He, R.; Xu, M.; Feng, S.; Li, S.; Zhou, L.; Mai, L. Silicon Oxides: A Promising Family of Anode Materials for Lithium-Ion Batteries. *Chem. Soc. Rev.* **2019**, *48* (1), 285–309.
- (5) Zhu, G.; Zhang, F.; Li, X.; Luo, W.; Li, L.; Zhang, H.; Wang, L.; Wang, Y.; Jiang, W.; Liu, H. K.; Dou, S. X.; Yang, J. Engineering the Distribution of Carbon in Silicon Oxide Nanospheres at the Atomic

Level for Highly Stable Anodes. *Angew. Chemie - Int. Ed.* **2019**, *58* (20), 6669–6673.

(6) Liu, T.; Yu, L.; Liu, J.; Lu, J.; Bi, X.; Dai, A.; Li, M.; Li, M.; Hu, Z.; Ma, L.; Luo, D.; Zheng, J.; Wu, T.; Ren, Y.; Wen, J.; Pan, F.; Amine, K. Understanding Co Roles towards Developing Co-Free Ni-Rich Cathodes for Rechargeable Batteries. *Nat. Energy* **2021**, *6* (3), 277–286.

(7) Zhang, H.; Liu, H.; Piper, L. F. J.; Whittingham, M. S.; Zhou, G. Oxygen Loss in Layered Oxide Cathodes for Li-Ion Batteries: Mechanisms, Effects, and Mitigation. *Chem. Rev.* **2022**, *122* (6), 5641–5681.

(8) Wang, L.; Liu, T.; Wu, T.; Lu, J. Strain-Retardant Coherent Perovskite Phase Stabilized Ni-Rich Cathode. *Nature* **2022**, *611* (7934), 61–67.

(9) Xu, G. L.; Liu, Q.; Lau, K. K. S.; Liu, Y.; Liu, X.; Gao, H.; Zhou, X.; Zhuang, M.; Ren, Y.; Li, J.; Shao, M.; Ouyang, M.; Pan, F.; Chen, Z.; Amine, K.; Chen, G. Building Ultraconformal Protective Layers on Both Secondary and Primary Particles of Layered Lithium Transition Metal Oxide Cathodes. *Nat. Energy* **2019**, *4* (6), 484–494.

(10) Chen, S.; Song, Z.; Wang, L.; Chen, H.; Zhang, S.; Pan, F.; Yang, L. Establishing a Resilient Conductive Binding Network for Si-Based Anodes via Molecular Engineering. *Acc. Chem. Res.* **2022**, *55* (15), 2088–2102.

(11) Oh, M. G.; Kwak, S.; An, K.; Tran, Y. H. T.; Kang, D. G.; Park, S. J.; Lim, G.; Kim, K.; Lee, Y. S.; Song, S. W. Perfluoro Macrocyclic Ether as an Ambifunctional Additive for High-Performance SiO and Nickel 88%-Based High-Energy Li-Ion Battery. *Adv. Funct. Mater.* **2023**, *33*, 2212890.

(12) Heiskanen, S. K.; Kim, J.; Lucht, B. L. Generation and Evolution of the Solid Electrolyte Interphase of Lithium-Ion Batteries. *Joule* **2019**, *3* (10), 2322–2333.

(13) Borodin, O.; Ren, X.; Vatamanu, J.; Von Wald Cresce, A.; Knap, J.; Xu, K. Modeling Insight into Battery Electrolyte Electrochemical Stability and Interfacial Structure. *Acc. Chem. Res.* **2017**, *50* (12), 2886–2894.

(14) Xu, K. Electrolytes and Interphases in Li-Ion Batteries and Beyond. *Chem. Rev.* **2014**, *114* (23), 11503–11618.

(15) Haregewoin, A. M.; Wotango, A. S.; Hwang, B. J. Electrolyte Additives for Lithium Ion Battery Electrodes: Progress and Perspectives. *Energy Environ. Sci.* **2016**, *9* (6), 1955–1988.

(16) von Aspern, N.; Rösenthaler, G. V.; Winter, M.; Cekic-Laskovic, I. Fluorine and Lithium: Ideal Partners for High-Performance Rechargeable Battery Electrolytes. *Angew. Chemie - Int. Ed.* **2019**, *58* (45), 15978–16000.

(17) Tan, S.; Shadik, Z.; Li, J.; Wang, X.; Yang, Y.; Lin, R.; Cresce, A.; Hu, J.; Hunt, A.; Waluyo, I.; Ma, L.; Monaco, F.; Cloetens, P.; Xiao, J.; Liu, Y.; Yang, X. Q.; Xu, K.; Hu, E. Additive Engineering for Robust Interphases to Stabilize High-Ni Layered Structures at Ultra-High Voltage of 4.8 V. *Nat. Energy* **2022**, *7* (6), 484–494.

(18) Etacheri, V.; Haik, O.; Goffer, Y.; Roberts, G. A.; Stefan, I. C.; Fasching, R.; Aurbach, D. Effect of Fluoroethylene Carbonate (FEC) on the Performance and Surface Chemistry of Si-Nanowire Li-Ion Battery Anodes. *Langmuir* **2012**, *28* (1), 965–976.

(19) Jin, Y.; Kneusels, N. J. H.; Marbella, L. E.; Castillo-Martinez, E.; Magusin, P. C. M. M.; Weatherup, R. S.; Jónsson, E.; Liu, T.; Paul, S.; Grey, C. P. Understanding Fluoroethylene Carbonate and Vinylene Carbonate Based Electrolytes for Si Anodes in Lithium Ion Batteries with NMR Spectroscopy. *J. Am. Chem. Soc.* **2018**, *140* (31), 9854–9867.

(20) Liao, B.; Li, H.; Xu, M.; Xing, L.; Liao, Y.; Ren, X.; Fan, W.; Yu, L.; Xu, K.; Li, W. Designing Low Impedance Interface Films Simultaneously on Anode and Cathode for High Energy Batteries. *Adv. Energy Mater.* **2018**, *8* (22), 1800802.

(21) Xu, G.; Pang, C.; Chen, B.; Ma, J.; Wang, X.; Chai, J.; Wang, Q.; An, W.; Zhou, X.; Cui, G.; Chen, L. Prescribing Functional Additives for Treating the Poor Performances of High-Voltage (5 V-Class) LiNi<sub>0.5</sub>Mn<sub>1.5</sub>O<sub>4</sub>/MCMB Li-Ion Batteries. *Adv. Energy Mater.* **2018**, *8* (9), 1701398.

- (22) Xiao, A.; Yang, L.; Lucht, B. L. Thermal Reactions of LiPF<sub>6</sub> with Added LiBOB. *Electrochem. Solid-State Lett.* **2007**, *10* (11), 241–244.
- (23) Morell, C.; Grand, A.; Toro-Labbé, A. New Dual Descriptor for Chemical Reactivity. *J. Phys. Chem. A* **2005**, *109* (1), 205–212.
- (24) Lu, T.; Chen, F. Bond Order Analysis Based on the Laplacian of Electron Density in Fuzzy Overlap Space. *J. Phys. Chem. A* **2013**, *117* (14), 3100–3108.
- (25) Sun, Q.; Cao, Z.; Ma, Z.; Zhang, J.; Wahyudi, W.; Cai, T.; Cheng, H.; Li, Q.; Kim, H.; Xie, E.; Cavallo, L.; Sun, Y. K.; Ming, J. Discerning Roles of Interfacial Model and Solid Electrolyte Interphase Layer for Stabilizing Antimony Anode in Lithium-Ion Batteries. *ACS Mater. Lett.* **2022**, *4* (11), 2233–2243.
- (26) Chen, Y.; Yu, Z.; Rudnicki, P.; Gong, H.; Huang, Z.; Kim, S. C.; Lai, J. C.; Kong, X.; Qin, J.; Cui, Y.; Bao, Z. Steric Effect Tuned Ion Solvation Enabling Stable Cycling of High-Voltage Lithium Metal Battery. *J. Am. Chem. Soc.* **2021**, *143* (44), 18703–18713.
- (27) Zou, Y.; Liu, G.; Wang, Y.; Li, Q.; Ma, Z.; Yin, D.; Liang, Y.; Cao, Z.; Cavallo, L.; Kim, H.; Wang, L.; Alshareef, H. N.; Sun, Y. K.; Ming, J. Intermolecular Interactions Mediated Nonflammable Electrolyte for High-Voltage Lithium Metal Batteries in Wide Temperature. *Adv. Energy Mater.* **2023**, *13*, 2300443.
- (28) Kim, K.; Hwang, D.; Kim, S.; Park, S. O.; Cha, H.; Lee, Y. S.; Cho, J.; Kwak, S. K.; Choi, N. S. Cyclic Aminosilane-Based Additive Ensuring Stable Electrode-Electrolyte Interfaces in Li-Ion Batteries. *Adv. Energy Mater.* **2020**, *10* (15), 1–12.
- (29) Jiang, G.; Liu, J.; He, J.; Wang, H.; Qi, S.; Huang, J.; Wu, D.; Ma, J. Hydrofluoric Acid-Removable Additive Optimizing Electrode Electrolyte Interphases with Li<sup>+</sup> Conductive Moieties for 4.5 V Lithium Metal Batteries. *Adv. Funct. Mater.* **2023**, *33* (12), 1–10.
- (30) Wang, Q.; Zhu, M.; Chen, G.; Dudko, N.; Li, Y.; Liu, H.; Shi, L.; Wu, G.; Zhang, D. High-Performance Microsized Si Anodes for Lithium-Ion Batteries: Insights into the Polymer Configuration Conversion Mechanism. *Adv. Mater.* **2022**, *34* (16), 1–13.
- (31) Qian, G.; Li, Y.; Chen, H.; Xie, L.; Liu, T.; Yang, N.; Song, Y.; Lin, C.; Cheng, J.; Nakashima, N.; Zhang, M.; Li, Z.; Zhao, W.; Yang, X.; Lin, H.; Lu, X.; Yang, L.; Li, H.; Amine, K.; Chen, L.; Pan, F. Revealing the Aging Process of Solid Electrolyte Interphase on SiOx Anode. *Nat. Commun.* **2023**, *14* (1), 6048.
- (32) Zhu, C.; Chen, S.; Li, K.; Yin, Z.-W.; Xiao, Y.; Lin, H.; Pan, F.; Yang, L. Quantitative Analysis of the Structural Evolution in Si Anode via Multi-Scale Image Reconstruction. *Sci. Bull.* **2023**, *68* (4), 408–416.
- (33) Prado, A. Y. R.; Rodrigues, M.-T. F.; Trask, S. E.; Shaw, L.; Abraham, D. P. Electrochemical Dilatometry of Si-Bearing Electrodes: Dimensional Changes and Experiment Design. *J. Electrochem. Soc.* **2020**, *167* (16), 160551.
- (34) Cheng, D.; Wynn, T. A.; Wang, X.; Wang, S.; Zhang, M.; Shimizu, R.; Bai, S.; Nguyen, H.; Fang, C.; Kim, M.; Li, W.; Lu, B.; Kim, S. J.; Meng, Y. S. Unveiling the Stable Nature of the Solid Electrolyte Interphase between Lithium Metal and LiPON via Cryogenic Electron Microscopy. *Joule* **2020**, *4* (11), 2484–2500.
- (35) Wu, F.; Dong, Y.; Su, Y.; Wei, C.; Chen, T.; Yan, W.; Ma, S.; Ma, L.; Wang, B.; Chen, L.; Huang, Q.; Cao, D.; Lu, Y.; Wang, M.; Wang, L.; Tan, G.; Wang, J.; Li, N. Benchmarking the Effect of Particle Size on Silicon Anode Materials for Lithium-Ion Batteries. *Small* **2023**, *2301301*, 1–17.
- (36) Zhang, Q.; Pan, J.; Lu, P.; Liu, Z.; Verbrugge, M. W.; Sheldon, B. W.; Cheng, Y. T.; Qi, Y.; Xiao, X. Synergetic Effects of Inorganic Components in Solid Electrolyte Interphase on High Cycle Efficiency of Lithium Ion Batteries. *Nano Lett.* **2016**, *16* (3), 2011–2016.
- (37) Fan, X.; Ou, X.; Zhao, W.; Liu, Y.; Zhang, B.; Zhang, J.; Zou, L.; Seidl, L.; Li, Y.; Hu, G.; Battaglia, C.; Yang, Y. In Situ Inorganic Conductive Network Formation in High-Voltage Single-Crystal Ni-Rich Cathodes. *Nat. Commun.* **2021**, *12* (1), 5320.
- (38) Yang, J.; Liu, X.; Wang, Y.; Zhou, X.; Weng, L.; Liu, Y.; Ren, Y.; Zhao, C.; Dahbi, M.; Alami, J.; Ei-Hady, D. A.; Xu, G. L.; Amine, K.; Shao, M. Electrolytes Polymerization-Induced Cathode-Electrolyte-Interphase for High Voltage Lithium-Ion Batteries. *Adv. Energy Mater.* **2021**, *11* (39), 2101956.
- (39) Gan, Q.; Qin, N.; Li, Z.; Gu, S.; Liao, K.; Zhang, K.; Lu, L.; Xu, Z.; Lu, Z. Surface Spinel Reconstruction to Suppress Detrimental Phase Transition for Stable LiNi<sub>0.8</sub>Co<sub>0.1</sub>Mn<sub>0.1</sub>O<sub>2</sub> Cathodes. *Nano Res.* **2023**, *16* (1), 513–520.
- (40) Ni, L.; Zhang, S.; Di, A.; Deng, W.; Zou, G.; Hou, H.; Ji, X. Challenges and Strategies towards Single-Crystalline Ni-Rich Layered Cathodes. *Adv. Energy Mater.* **2022**, *12*, 2201510.
- (41) Chang, B.; Kim, J.; Cho, Y.; Hwang, I.; Jung, M. S.; Char, K.; Lee, K. T.; Kim, K. J.; Choi, J. W. Highly Elastic Binder for Improved Cyclability of Nickel-Rich Layered Cathode Materials in Lithium-Ion Batteries. *Adv. Energy Mater.* **2020**, *10*, 2001069.
- (42) Yu, T.; Zhao, T.; Zhang, N.; Xue, T.; Chen, Y.; Ye, Y.; Wu, F.; Chen, R. Spatially Confined LiF Nanoparticles in an Aligned Polymer Matrix as the Artificial SEI Layer for Lithium Metal Anodes. *Nano Lett.* **2023**, *23* (1), 276–282.
- (43) Chen, J.; Fan, X.; Li, Q.; Yang, H.; Khoshi, M. R.; Xu, Y.; Hwang, S.; Chen, L.; Ji, X.; Yang, C.; He, H.; Wang, C.; Garfunkel, E.; Su, D.; Borodin, O.; Wang, C. Electrolyte Design for LiF-Rich Solid-Electrolyte Interfaces to Enable High-Performance Microsized Alloy Anodes for Batteries. *Nat. Energy* **2020**, *5* (5), 386–397.
- (44) Zhang, J. N.; Li, Q.; Wang, Y.; Zheng, J.; Yu, X.; Li, H. Dynamic Evolution of Cathode Electrolyte Interphase (CEI) on High Voltage LiCoO<sub>2</sub> Cathode and Its Interaction with Li Anode. *Energy Storage Mater.* **2018**, *14*, 1–7.
- (45) Zhao, W.; Zheng, G.; Ji, Y.; Peng, C.; Ren, F.; Liu, M.; Pan, F.; Yang, Y. Modulation and Quantitative Study of Conformal Electrode-Electrolyte Interfacial Chemistry toward High-Energy-Density LiNi<sub>0.6</sub>Co<sub>0.2</sub>Mn<sub>0.2</sub>O<sub>2</sub>||SiO-C Pouch Cells. *Energy Storage Mater.* **2022**, *53*, 424–434.
- (46) Xu, J.; Zhang, J.; Pollard, T. P.; Li, Q.; Tan, S.; Hou, S.; Wan, H.; Chen, F.; He, H.; Hu, E.; Xu, K.; Yang, X. Q.; Borodin, O.; Wang, C. Electrolyte Design for Li-Ion Batteries under Extreme Operating Conditions. *Nature* **2023**, *614* (7949), 694–700.
- (47) Lu, T.; Chen, F. Multiwfn: A Multifunctional Wavefunction Analyzer. *J. Comput. Chem.* **2012**, *33* (5), 580–592.